ACS OMEGA

http://pubs.acs.org/journal/acsodf

Article

The Preparation of $CuInS_2$-ZnS-Glutathione Quantum Dots and Their Application on the Sensitive Determination of Cytochrome *c* and Imaging of HeLa Cells

Xiangyang An, Yuemei Zhang, Jing Wang, De-ming Kong, Xi-wen He, Langxing Chen,* and Yukui Zhang

Cite This: *ACS Omega* 2021, 6, 17501−17509

Read Online

ACCESS | Metrics & More | Article Recommendations | Supporting Information

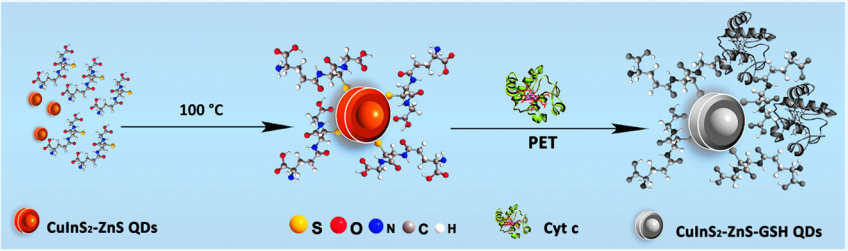

ABSTRACT: Cytochrome *c* (Cyt *c*), one of the most significant proteins acting as an electron transporter, plays an important role during the transferring process of the energy in cells. Apoptosis, one of the major forms of cell death, has been associated with various physiological regularity and pathological mechanisms. It was found that Cyt *c* can be released from mitochondria to cytosol under different pathological conditions, triggering subsequent cell apoptosis. Herein, we developed a fluorescence nanoprobe based on negatively charged $CuInS_2$-ZnS-GSH quantum dots (QDs) for the sensitive determination of Cyt *c*. $CuInS_2$-ZnS-GSH QDs with high photochemical stability and favorable hydrophilicity were prepared by a simple hot reflux method and emit a bright orange-red light. The electron-deficient heme group in Cyt *c* is affiliated with the electron-rich $CuInS_2$-ZnS-GSH QDs through the photo-induced electron transfer process, resulting in a large decrease in fluorescence intensity of QDs. A good linearity for concentration of Cyt *c* in the range of 0.01−7 μmol L^{-1} is obtained, and the detection limit of Cyt *c* is as low as 1.1 nM. The performance on the detection of Cyt *c* in spiked human serum and fetal bovine serum samples showed good recoveries from 85.5% to 95.0%. Furthermore, $CuInS_2$-ZnS-GSH QDs were applied for the intracellular imaging in HeLa cells showing an extremely lower toxicity and excellent biocompatibility.

1. INTRODUCTION

Cytochrome *c* (Cyt *c*) is a water-soluble protein consisting of a single polypeptide chain of 104 amino acid residues and a heme group, which is located in the intermembrane space of mitochondria.[1] Cyt *c* acts as an electron transporter in the biological oxidation process, plays an important role in transferring energy, and enhances the utilization of oxygen in hypoxia organisms. Apoptosis,[2−4] one of the major forms of cell death, has been associated with various physiological regularity and pathological mechanisms such as immune response, tumors, liver diseases, and cardiovascular autoimmune diseases. A number of studies have indicated that Cyt *c* can be released from mitochondria to cytosol under different pathological conditions, triggering subsequent cell apoptosis.[5−8] In the last few decades, it was confirmed that Cyt *c* not only can be released into cytosol of cells but also leaves the cells and reaches into the blood circulation of patients, those who suffer from cardiac arrest, myocardial infarction, and cancer therapy.[9,10] Therefore, the analysis of Cyt *c* can be a critical factor to understand cell apoptosis and evaluate the efficacy of therapy toward clinical treatment. Among the methods for analysis of Cyt *c*, high-performance liquid chromatography (HPLC),[11] electrophoresis,[12] and enzyme-linked immunosorbent assay (ELISA)[13] suffered from time-consuming and complex operation. In recent years, fluorescence spectroscopy technology[14−16] has been developed rapidly due to its short analysis time, relatively easy operation, and low cost, providing an attractive alternative for Cyt *c* determination.

With increasing global attention on semiconductor materials, quantum dots (QDs), which are inorganic semiconductor nanocrystals (typically 2−10 nm in diameter), have a high

Received: April 13, 2021
Accepted: June 18, 2021
Published: June 30, 2021

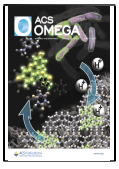

https://doi.org/10.1021/acsomega.1c01983
ACS Omega 2021, 6, 17501−17509

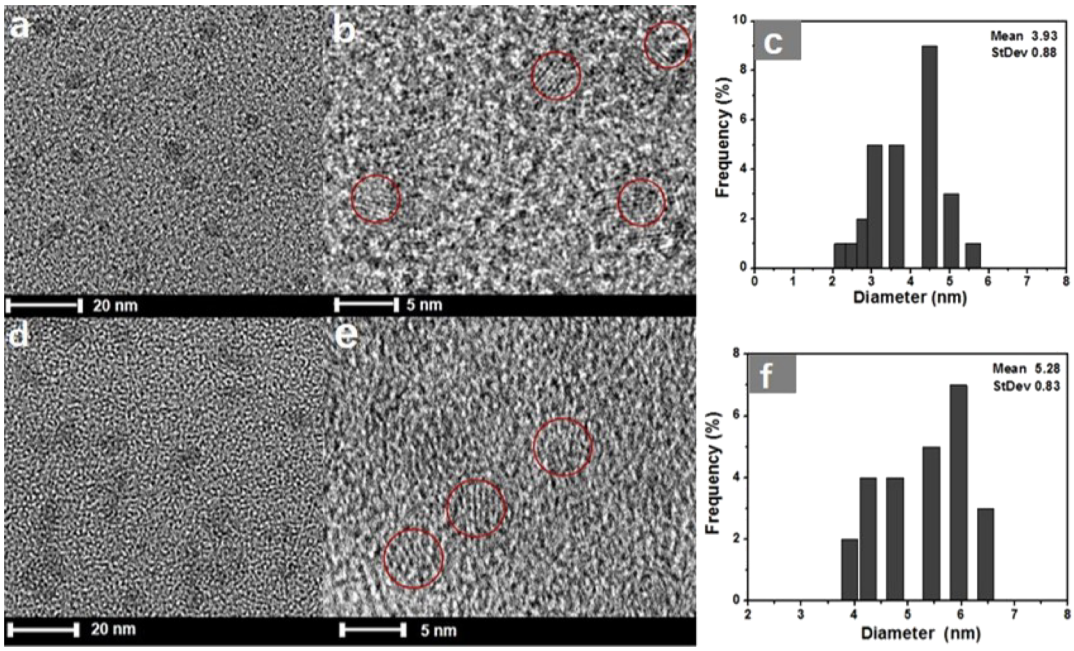

Figure 1. (a) TEM, (b) HR-TEM, and (c) particle size distribution of $CuInS_2$ QDs and (d) TEM, (e) HR-TEM, and (f) particle size distribution of $CuInS_2$-ZnS-GSH QDs.

emission quantum yields, broad absorption spectra, photochemical stability, and PL properties that are controllable by varying their particle size.[17−20] In recent years, QDs have been widely used in batteries, photovoltaics, light-emitting diodes, fluorescent labeling, sensing, and biological imaging systems due to their unique optical properties.[21−26] Most binary compounds-based traditional semiconductor QDs usually contain heavy metal elements (Cd, Pb, and Hg) and have a destructive impact on the environment due to its toxicity, which has become a major limitation on the use of QDs.[27] The development of less toxic and green QDs is attractive. Several eco-friendly QDs such as carbon dots, graphene dots, and heavy metal-free QDs like ZnO, ZnS, $CuInS_2$, $CuInS_2$/ZnS, and $AgInS_2$ QDs have been successfully synthesized and applied in biological and healthcare fields.[28−32]

$CuInS_2$ QDs, as the I−III−VI ternary semiconductor nanocrystals containing two cations (Cu^+ and In^{3+}) and one anion (S^{2-}), possess several significant advantages, such as large Stokes shift, versatile chemical modifications, and various emission wavelengths, which have aroused enormous research interest.[26,33] The emission wavelength of $CuInS_2$ QDs can be tuned from the visible to the NIR region by both the size and the composition of QDs.[34−36] Furthermore, their photoluminescence properties can be improved by modifying the $CuInS_2$ QDs surface with the growth of the ZnS shell to form a $CuInS_2$/ZnS core/shell structure, where the ZnS shell effectively passivates surface defects causing nonradiative recombination.[33,35] Up to now, some strategies[37−43] such as hot-injection, thermolysis, microwave-assisted, as well as solvothermal methods have been reported to prepare $CuInS_2$ or $CuInS_2$/ZnS core/shell QDs. However, most of the approaches have some drawbacks, such as high temperature, poor water solubility, and using organic solvents. Similar to the hydrothermal method, the hot reflux method is performed in the aqueous phase under normal pressure, which is easy to be operated and low cost.

Herein, negatively charged core−shell $CuInS_2$-ZnS-GSH QDs were prepared by a simple hot reflux method in aqueous solution. $CuInS_2$-ZnS-GSH QDs possess outstanding water solubility and biocompatibility to accompany the improvement of stability and lifetime. Owing to the electron-deficient heme groups existing, Cyt *c* can act as an efficient quencher for $CuInS_2$-ZnS-GSH QDs through the photo-induced electron transfer process (PET). The thiol-based ligands are widely used to synthesize highly efficient and stable QDs with relatively simple steps.[44] Glutathione (GSH) is chosen as the reductant, electron donor, and stabilizer. The isoelectronic points are 5.93 for GSH and 10.83 for Cyt *c*. The negatively charged $CuInS_2$-ZnS-GSH QDs will exhibit the electrostatic interaction with positively charged Cyt *c* in the weak alkaline solution (pH 9), which is further beneficial to the photo-induced electron transfer (PET). The PET results in the fluorescence quenching of $CuInS_2$-ZnS-GSH QDs, and the fluorescence quenching intensity is linear to the concentration of Cyt *c*. In addition, the mean photoluminescence (PL) lifetime value of $CuInS_2$-ZnS-GSH QDs is 214.4 ns, which is longer than that of most organic dyes, thus can be good candidates for long-term fluorescent imaging. Therefore, a highly sensitive and selective fluorescent sensor based on $CuInS_2$-ZnS-GSH QDs was developed for Cyt *c* detection in serum samples. The application of $CuInS_2$-ZnS-GSH QDs on intracellular imaging in HeLa cells with lower toxicity and excellent biocompatibility was also demonstrated in this work.

2. RESULTS AND DISCUSSION

2.1. Characterization of $CuInS_2$-ZnS-GSH QDs. The morphology and structure of $CuInS_2$ QDs and $CuInS_2$-ZnS-GSH QDs were analyzed by biological freezing transmission electron microscopy (TEM). The TEM image of the $CuInS_2$ QDs is presented in Figure 1a, showing that the nanocrystals are well dispersed and their average size is 3.9 nm. After modification with the ZnS shell, the morphology of $CuInS_2$-ZnS-GSH QDs (Figure 1d) is obviously observed with the

https://doi.org/10.1021/acsomega.1c01983
ACS Omega 2021, 6, 17501−17509

average diameter of ~5.3 nm, which is a little thicker than that of the original $CuInS_2$ QDs. The high-resolution TEM (HR-TEM) images (Figure 1b,e) exhibit the crystalline structure and lattice plane of QDs. Figure 1c−f shows the histogram of size distribution image of $CuInS_2$ QDs and $CuInS_2$-ZnS-GSH QDs, respectively.

An FT-IR spectrometer was used to identify the functional groups on the surface of $CuInS_2$-ZnS-GSH QDs in the range of 400−4000 cm^{-1} (Figure S1, Supporting Information). The peaks at 2921 and 2824 cm^{-1} are the stretching vibration of the $-CH_2$ group. Meanwhile, the wide spectra ranged from 3300 to 3500 cm^{-1} are assigned to −NH and COO^- vibration. The absorption band at 1712, 1538, 1630, and 1396 cm^{-1} is attributed to the characteristic band −C═O, −N−H, $-NH_2$, and −C−N, respectively. According to the curve S1a in the FT-IR spectra, an obvious peak at 2525 cm^{-1} resulted from the stretching vibration of −SH in free GSH,[45] while the unique absorption band disappears in the spectra of $CuInS_2$-ZnS-GSH QDs (curve S1b, Supporting Information). This can be explained by the fact that the −SH groups in GSH have formed the chemical bonds with metals in $CuInS_2$-ZnS-GSH QDs.

The crystalline phase of QDs was identified by X-ray diffraction (XRD). As shown in Figure S2a (Supporting Information), three diffraction peaks at 27.38°, 46.50°, and 54.41° from $CuInS_2$ QDs are well matched with the standard XRD data of chalcopyrite $CuInS_2$ (JCSD: 01-085-1575), which is assigned to (111), (220), and (311) planes, respectively. In comparison with $CuInS_2$ QDs, the three major peaks in the XRD pattern of $CuInS_2$-ZnS-GSH QDs (Figure S2b, Supporting Information) are moved slightly to the higher angle, which are located between chalcopyrite $CuInS_2$ and ZnS phases (JCSD: 01-077-2100).[46] The results indicate that the ZnS shell was coated on the surface of $CuInS_2$ QDs.

To further confirm the constituent elements and valence state of $CuInS_2$-ZnS-GSH QDs, the X-ray photoelectron spectroscopy (XPS) analysis was carried out. As depicted in Figure 2a, the In 3d, Cu 2p, Zn 2p, N 1s, and S 2p levels are all successfully observed. The element (In, Cu, Zn, N, and S) content in $CuInS_2$-ZnS-GSH QDs was estimated with the ratio of 14.96, 3.33, 24.76, 26.29, and 30.66%, respectively. The Cu 2p XPS spectrum in Figure 2b is split into two peaks at 445.4 and 453 eV with a standard separation of 7.6 eV, indicating that the valence state of Cu ion is +1, and the precursor $CuCl_2$ is reduced into Cu(I) by GSH. In the high-resolution In 3d XPS spectrum (Figure 2c), the two peaks at 444.6 and 452.1 eV suggest that the state of indium in $CuInS_2$-ZnS-GSH QDs is +3. HR-XPS spectra in Figure 2d−f also confirm the valences states of S^{2-} (S $2p_{3/2}$, 161.4 eV), N^{3-} (N 1s, 399.3 eV), and Zn^{2+} (Zn $2p_{3/2}$, 1021.6 eV; Zn $2p_{1/2}$, 1044.5 eV), proving the successful modification of GSH and the perfect coating of the ZnS shell in $CuInS_2$-ZnS-GSH QDs.[37,39]

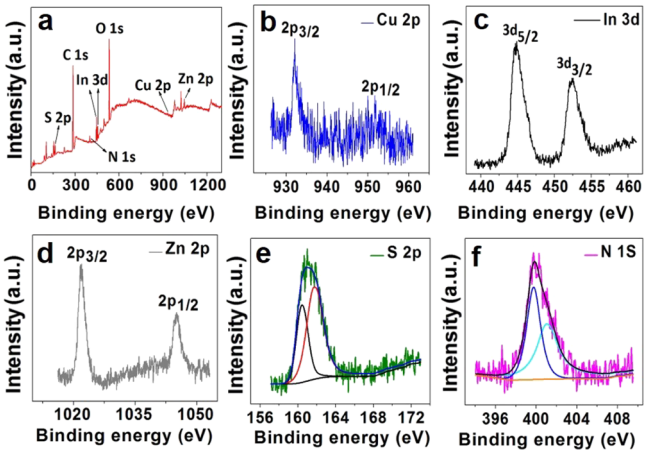

Figure 2. XPS survey spectra of $CuInS_2$-ZnS-GSH QDs (a) and high-resolution spectra of Cu 2p (b), In 3d (c), Zn2p (d), S 2p (e), and N 1s (f) of $CuInS_2$-ZnS-GSH QDs.

2.2. Optical Properties of QDs. The UV−vis absorption and normalized photoluminescence emission spectra of QDs are illustrated in Figure 3A,B. It is found that the UV−vis absorption peak of $CuInS_2$-ZnS QDs is at 448 nm (Figure 3A). The $CuInS_2$-ZnS-Cys and $CuInS_2$-ZnS-GSH QDs have a wide range of absorption and its maximum photoluminescence emission wavelength (Figure 3B) is around 640 nm. From the inset pictures (a−d), $CuInS_2$, $CuInS_2$-ZnS, $CuInS_2$-ZnS-Cys, and $CuInS_2$-ZnS-GSH QDs all exhibit a bright orange-red color under the 365 nm irradiation light. The influence of the ZnS shell on the optical properties of $CuInS_2$ QDs was investigated. From left to right (A−D) in Figure S3 (Supporting Information), it is found that the color of $CuInS_2$-ZnS-GSH QDs is changed from orange-red to blue by different amounts of ZnS shells, displaying an interesting optical property. The brightest QDs were obtained when the molar ratio of Cu^{2+} and Zn^{2+} precursor was 1:8. Furthermore, an absolute photoluminescence quantum yield (PLQY) of 13% was estimated for $CuInS_2$-ZnS-GSH QDs in PBS solution.

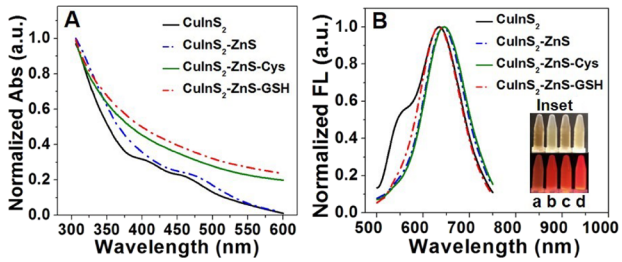

Figure 3. (A) UV−vis absorption spectra and (B) PL emission of $CuInS_2$, $CuInS_2$-ZnS, and $CuInS_2$-ZnS-Cys QDs. The inset pictures are $CuInS_2$, $CuInS_2$-ZnS, $CuInS_2$-ZnS-Cys, and $CuInS_2$-ZnS-GSH QDs under incandescent light at 365 nm.

The hydrodynamic diameter (HD) of QDs was measured by the dynamic light scattering (DLS) technique. The HDs from the DLS data are 4.4 nm for $CuInS_2$ QDs (Figure S4a, Supporting Information) and 5.7 nm for $CuInS_2$-ZnS-GSH QDs (Figure S4b, Supporting Information). The diameter obtained from DLS is a little larger than that obtained by TEM analysis. As shown in Figure S4c (Supporting Information), the zeta potential values of $CuInS_2$-ZnS-GSH QDs and $CuInS_2$-ZnS-Cys QDs are −35.2 and −29.2 mV, respectively. Furthermore, the change in fluorescence intensity of $CuInS_2$-ZnS-GSH QDs in the PBS solution over a 15 day period was evaluated. As depicted in Figure S4d (Supporting Information), the $CuInS_2$-ZnS-GSH QDs did not exhibit a significantly reduced PL intensity and kept the colloidal stability in a refrigerator at 4 °C. Besides DLS and zeta potential characterizations, the PL lifetime measurements of $CuInS_2$-ZnS-GSH QDs were also conducted (Figure S5, Supporting Information). The PL decay curve of these $CuInS_2$-ZnS-GSH QDs could be fitted well using the bi-exponential model, with a

https://doi.org/10.1021/acsomega.1c01983
ACS Omega 2021, 6, 17501−17509

fast lifetime τ_1 = 38.8 ns and a slow lifetime τ_2 = 240.1 ns, which can be assigned to surface trap states and donor−acceptor transition of trap states, respectively. In order to validate the feasibility, the PL lifetime of $CuInS_2$-ZnS-GSH QDs in the Cyt *c* solution was also measured. The mean PL lifetime value of $CuInS_2$-ZnS-GSH QDs was changed from 214.4 to 149.7 ns, indicating a strong reaction between Cyt *c* and $CuInS_2$-ZnS-GSH QDs (Table S1, Supporting Information). The mean PL lifetime remains almost the same when the $CuInS_2$-ZnS-GSH QDs were dispersed in the BSA solution, suggesting that the fluorescence quenching of these QDs is more dependent on the PET process.

2.3. Fluorescence Response toward Cyt *c*. The effect of pH on the fluorescence quenching of $CuInS_2$-ZnS-GSH QDs was investigated. As shown in Figure S6a (Supporting Information), the fluorescence intensity of original $CuInS_2$-ZnS-GSH QDs exhibits a gradual increase in the pH range of 4−10 because the stability of the ZnS shell is better in the alkaline solution. After Cyt *c* was added in $CuInS_2$-ZnS-GSH QDs, the intensity of fluorescence decreased sharply. The incubated time of $CuInS_2$-ZnS-GSH QDs in the presence of Cyt *c* was also investigated. The fluorescence intensity of QDs decreased greatly from 0 to 1 min (Figure S6b, Supporting Information) and remained constant after 3 min. The optimal incubated time of 4 min was chosen in the subsequent experiment.

To confirm the effect of different stabilizers and electron donors on the determination of Cyt *c*, the $CuInS_2$-ZnS-GSH QDs and $CuInS_2$-ZnS-Cys QDs coated respectively with GSH and Cys were systematically investigated. As shown in Figure 4a, the fluorescence intensity of $CuInS_2$-ZnS-GSH QDs decreases obviously along with the increase in Cyt *c* concentration, indicating that this system can be used as a determination probe for Cyt *c*. The $CuInS_2$-ZnS-GSH QDs fluorescent nanoprobe (Figure 4b) has a linear range of 0.01−7 μmol L^{-1}, following a linear equation F_0/F = 1.031 + 0.551[Cyt *c*] (μmol L^{-1}) with a correlation coefficient of 0.998, and its detection limit for Cyt *c* is 1.1 nM. The detection limit is defined by the equation LOD = $3\sigma/k$, where σ is the standard deviation of the blank signals of $CuInS_2$-ZnS-GSH QDs, and k is the slope of the calibration curve. Similar to $CuInS_2$-ZnS-GSH QDs, the fluorescence intensity of $CuInS_2$-ZnS-Cys QDs also decreases along with the increase in Cyt *c* concentration (Figure 4c). The Cyt *c* concentration ranged from 0.02 to 3 μmol L^{-1} with a linear equation of F_0/F = 0.684 + 1.033[Cyt *c*] (μmol L^{-1}), its correlation coefficient is 0.996, and the detection limit is 1.7 nM (Figure 4d). In comparison with $CuInS_2$-ZnS-Cys QDs, $CuInS_2$-ZnS-GSH QDs with GSH as the stabilizer has a lower detection limit and a wider linear range than $CuInS_2$-ZnS-Cys QDs with Cys as the stabilizer.

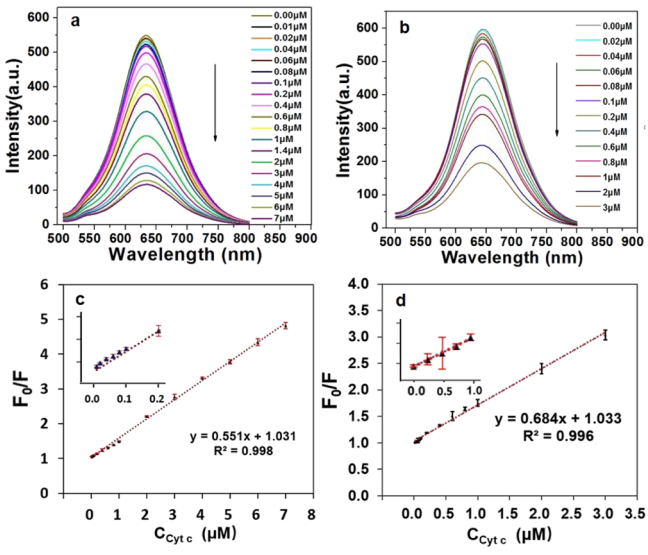

Figure 4. Fluorescence spectra of $CuInS_2$-ZnS-GSH QDs (a) and $CuInS_2$-ZnS-Cys QDs (b) in the presence of various concentrations of Cyt *c* in PBS aqueous solution (pH 9). Calibration graph of $CuInS_2$-ZnS-GSH QDs (c) and $CuInS_2$-ZnS-Cys QDs (d) for Cyt *c* detection. The error bars represent the standard deviations from the mean of three independent experiments.

The mechanism for the determination of Cyt *c* can be ascribed to the photo-induced electron transfer process. The change in fluorescent intensity is mainly dependent on the conjugation of GSH-capped $CuInS_2$-ZnS QDs with Cyt *c* forming a QDs−Cyt *c* composite system. Owing to the electron-deficient heme groups existing in the structure of Cyt *c*, Cyt *c* can act as an efficient quencher through photo-induced electron transfer process between Cyt *c* and electron-rich $CuInS_2$-ZnS-GSH QDs, resulting in a large decrease in fluorescence intensity of QDs.

The zeta potential values of $CuInS_2$-ZnS-GSH QDs and $CuInS_2$-ZnS-Cys QDs in PBS (pH 9.0) are −35.2 and −29.2 mV, respectively. Because GSH-capped $CuInS_2$-ZnS QDs has more negative charge than that of $CuInS_2$-ZnS-Cys QDs, the electrostatic interaction between $CuInS_2$-ZnS-GSH QDs with Cyt *c* is stronger. Therefore, as a modifier, GSH is more suitable than Cys to apply in the determination of Cyt *c*. In addition, the detection limit of $CuInS_2$-ZnS-GSH QDs as a nanoprobe for determination of Cyt *c* is lower than most of the designed methods (Table S2, Supporting Information).[8,11,15,16,47−50]

2.4. Specificity for Cyt *c* Detection. Owing to some proteins such as Mb and the Mb-containing heme porphyrin structure, the selectivity response of $CuInS_2$-ZnS-GSH QDs toward Cyt *c*, Mb, Hb, and a common protein BSA at different pH values was investigated. As shown in Figure S7a (Supporting Information), the fluorescence intensity of $CuInS_2$-ZnS-GSH QDs shows almost no change in the presence of BSA along with the pH value that increased from 6 to 10. The reason is that BSA has no heme porphyrin in the chemical structure, so no PET process between BSA and $CuInS_2$-ZnS-GSH QDs existed. However, the slight fluorescence quenching of $CuInS_2$-ZnS-GSH QDs in the presence of proteins containing heme porphyrin like Mb and Hb $CuInS_2$-ZnS-GSH QDs was observed in the range of pH 6−10. This is attributed to the fact that Hb and Mb will take some negative charges at pH 9 because the isoelectronic points of Mb and Hb are 6.99 and 7.07, respectively. The existing electrostatic repulsion between Mb (Hb) and negatively charged $CuInS_2$-ZnS-GSH QDs can impede the PET process. The fluorescence quenching intensity of $CuInS_2$-ZnS-GSH QDs to Cyt *c* is over four times than the other proteins. The results demonstrated that the $CuInS_2$-ZnS-GSH QDs exhibit a high selectivity to Cyt *c* in comparison with proteins Mb, Hb, and BSA at the weak alkaline solution. To further investigate the selectivity of $CuInS_2$-ZnS-GSH QDs for Cyt *c* determination, the response of $CuInS_2$-ZnS-GSH QDs to several other species such as amino acids, urea, sugar, metal ions, and anion is also exhibited in Figure S7b (Supporting Information). After each of Cys,

https://doi.org/10.1021/acsomega.1c01983
ACS Omega 2021, 6, 17501−17509

Glc, Asp, Tyr, Lys, Thr, Ser, Arg, Glu, ATP, urea, Fe^{3+}, Na^{+}, K^{+}, Fe^{2+}, Ca^{2+}, Mg^{2+}, CO_3^{2-}, Cl^{-}, SO_4^{2-}, NO_3^{-}, BSA, Hb, HSA, Mb, Lyz, IgG, and Cyt *c* was dispersed in the $CuInS_2$-ZnS-GSH QDs solution, quenching in the fluorescence intensity of QDs resulting from Cyt *c* is the biggest. The results indicated the high selectivity of $CuInS_2$-ZnS-GSH QDs for Cyt *c* determination.

To investigate the anti-interference ability of $CuInS_2$-ZnS-GSH QDs to Cyt *c*, several other species such as amino acids, urea, sugar, metal ions, and anion on the detection of Cyt *c* were measured. As shown in Figure 5, there is no significant change in the fluorescence signal of $CuInS_2$-ZnS-GSH QDs in the solution containing Cyt *c* and interfering substances. The proteins such as BSA, Hb, Mb, HSA, Lyz, and IgG were chosen to evaluate the interference on the determination of Cyt *c* because of Mb and the Mb-containing heme porphyrin structure like Cyt *c*, BSA, HSA, and IgG as high abundant proteins in the serum sample and Lyz having a near isoelectronic point with Cyt *c*. The results in Figure 5 indicated that most small biomolecules, ions, and proteins did not produce noticeable effects on the determination of Cyt *c* using the $CuInS_2$-ZnS-GSH QDs as a nanoprobe.

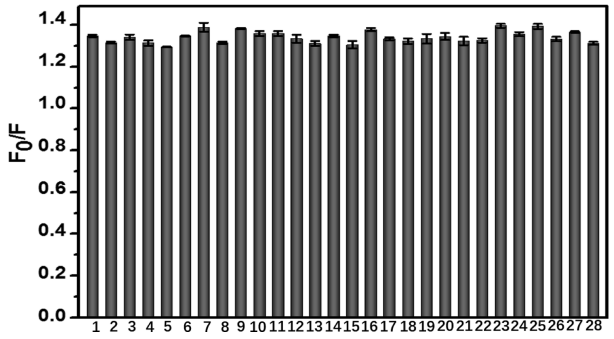

Figure 5. Selectivity of $CuInS_2$-ZnS-GSH QDs for Cyt *c* determination. From column 1 to 11, Cyt *c* is mixed with different small biomolecules (Cys, Glc, Asp, Tyr, Lys, Thr, Ser, Arg, Glu, ATP, or urea) in a solution at a molar concentration ratio of 1:500. From column 12 to 21, Cyt *c* is mixed with different ions (Fe^{3+}, Na^{+}, K^{+}, Fe^{2+}, Ca^{2+}, Mg^{2+}, CO_3^{2-}, Cl^{-}, SO_4^{2-}, or NO_3^{-}) at a molar concentration ratio of 1:200. From column 22 to 27, Cyt *c* is mixed with different proteins (BSA, Hb, HSA, Mb, Lyz, or IgG) at a molar concentration ratio of 1:5. Column 28 is only Cyt *c* without other interferences. The concentration of Cyt *c* is fixed at 0.4 μmol L^{-1}. The error bars represent the standard deviations from the mean of three independent experiments.

2.5. Live Cell Imaging of Cyt *c* Release. The toxicity of $CuInS_2$-ZnS-GSH QDs in HeLa cells was determined by MTT assays. With a wide concentration range of 15−100 μg mL^{-1}, $CuInS_2$-ZnS-GSH QDs were incubated with HeLa cells for 24 h at 37 °C. As illustrated in Figure S8 (Supporting Information), the cell viabilities are 85.9, 94.3, 96.5, and 97.3%, respectively, and the results show that $CuInS_2$-ZnS-GSH QDs possess an extremely lower toxicity and excellent biocompatibility.

To further evaluate the availability of $CuInS_2$-ZnS-GSH QDs in cell imaging, HeLa cells were used for monitoring the release of Cyt *c* from mitochondria.[51] Because Cyt *c* is located in the mitochondrial intermembrane/intercristal spaces of living cells, the mitochondrion membrane will separate Cyt *c* from $CuInS_2$-ZnS-GSH QDs. After being incubated with $CuInS_2$-ZnS-GSH QDs for 2 h, HeLa cells show a strong fluorescence emission, and it was found that the $CuInS_2$-ZnS-GSH QDs entered the cells (Figure 6A). Etoposide, as an effective apoptosis inducer, can specifically lead to the release of Cyt *c* from mitochondria to cytosol in apoptotic cells.[52] As can be seen from Figure 6A−D, the fluorescence intensity of HeLa cells is gradually decreased with the increase in etoposide concentration. In addition, as illustrated in bright-field images (Figure 6a−d), the morphology of HeLa cells changed from

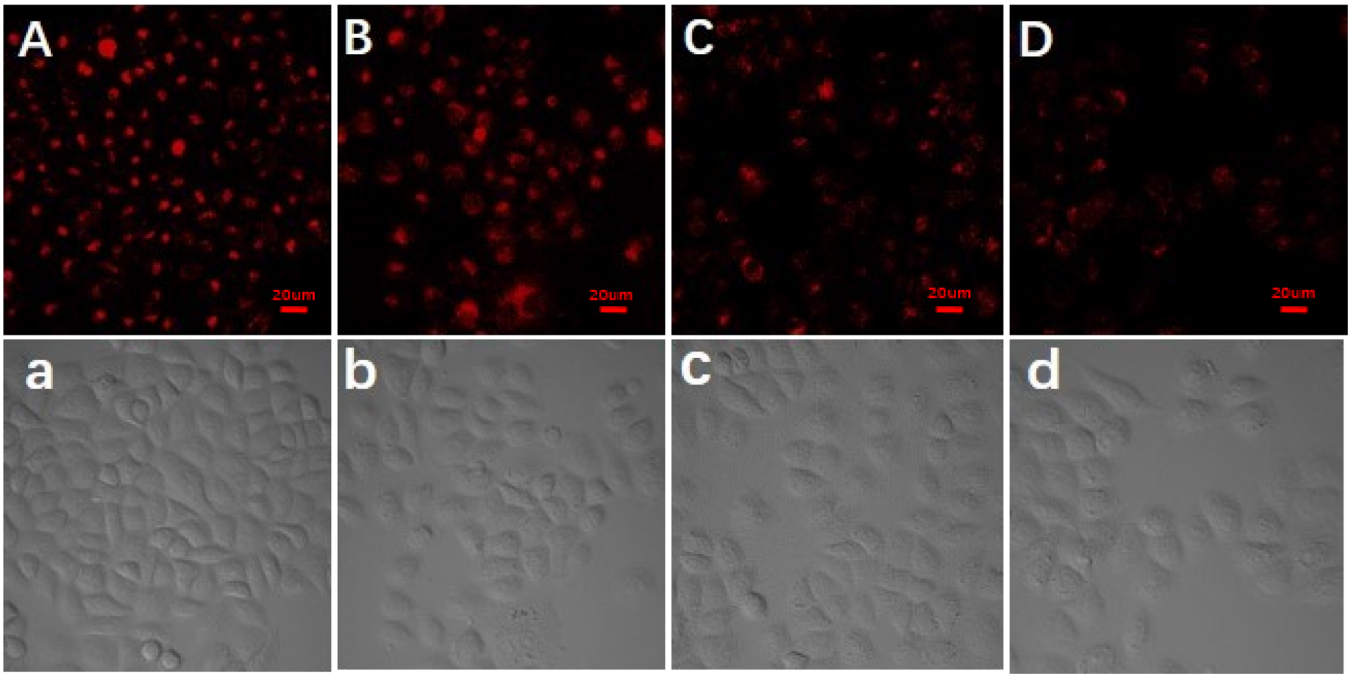

Figure 6. Fluorescence imaging of $CuInS_2$-ZnS-GSH QDs stained HeLa cells treated with different concentrations of etoposide for 2 h. From (A) to (D), the concentrations of etoposide were 0, 10, 50, and 100 μmol L^{-1}, respectively. The matched bright-field images (a−d) were also obtained. The scale bars indicate 20 μm.

https://doi.org/10.1021/acsomega.1c01983
ACS Omega 2021, 6, 17501−17509

the tridimensional to flat state, suggesting the release of Cyt *c* during the process of etoposide-induced cell apoptosis. As a result, the $CuInS_2$-ZnS-GSH QDs have features of excellent biocompatibility and high fluorescence intensity, making them a superior candidate in potential cell imaging. In addition, the fluorescence emission intensity almost did not change after the addition of different concentrations of etoposide (0, 10, 50, and 100 μM) in Figure S9 (Supporting Information), indicating that the change in probe fluorescence intensity is not caused by etoposide.

2.6. Application to Real Sample Analysis. In order to investigate the practicability of the developed $CuInS_2$-ZnS-GSH QDs sensing system in real sample analysis, the performance on the detection of Cyt *c* in spiked human serum and fetal bovine serum samples was investigated and is shown in Table 1. The recoveries of Cyt *c* spiked with the concentrations closer to the actual physiological range in human serum samples and in FBS samples were obtained in the range of 87.8−94.0% and 85.5−95.0%, respectively. The results exhibited that serum matrices have no obvious interference in the determination of Cyt *c* by the fluorescent $CuInS_2$-ZnS-GSH QDs, suggesting a promising application in real biological samples.

Table 1. Detection of Cyt *c* in Human Serum or Fetal Bovine Serum Samples

	Cyt *c* concentration (μM)		
sample	added	measured (mean ± std, n = 3)	recovery (%) (mean ± std, n = 3)
human serum	0.10	0.18 ± 0.01	90 ± 6.6
	2.00	2.15 ± 0.04	105 ± 2.1
fetal bovine serum	0.10	0.19 ± 0.01	102 ± 5.2
	2.00	2.12 ± 0.04	106 ± 2.0

3. CONCLUSIONS

In summary, negatively charged $CuInS_2$-ZnS-GSH QDs were prepared by a simple hot reflux method and were applied for sensitive determination of Cyt *c* and bioimaging. The fluorescent $CuInS_2$-ZnS-GSH QDs show a high selectivity toward Cyt *c* even in the presence of other strong interfering proteins such as Mb, Hb, and BSA. A good recovery is obtained in spiked human serum and fetal bovine serum samples. Due to its special advantage of small size, excellent biocompatibility, and low toxicity, $CuInS_2$-ZnS-GSH QDs also show superior imaging in HeLa cells. The results demonstrated that $CuInS_2$-ZnS-GSH QDs are a promising fluorescent sensor for monitoring the release of Cyt *c* from mitochondria.

4. EXPERIMENTAL SECTION

4.1. Reagents and Materials. Cyt *c* was purchased from Sigma-Aldrich (USA). Indium(III) chloride tetrahydrate ($InCl_3{\cdot}4H_2O$) and copper(II) chloride dihydrate ($CuCl_2{\cdot}2H_2O$) were purchased from Energy Chemical (Shanghai, China). Myoglobin (Mb), hemoglobin (Hb), bovine serum albumin (BSA), human serum albumin (HSA), immunoglobulin G (IgG), lysozyme (Lyz), glutathione (GSH), adenosine triphosphate (ATP), etoposide, and human serum were purchased from Solarbio (Beijing, China). Zinc acetate ($Zn(Ac)_2$) was purchased from Meryer Chemical Technology Co., Ltd. (Shanghai, China). Human cervical cancer cell line (HeLa) was obtained from the Cell Bank of Type Culture Collection of the Chinese Academy of Sciences (Shanghai, China). Penicillin, fetal bovine serum (FBS), streptomycin, and Dulbecco's modified Eagle's medium (DMEM) were purchased from Gibco (Thermo Fisher Scientific). 3-(4,5-Dimethylthiazol-2-yl)-2,5-diphenyltetrazolium bromide (MTT) was purchased from Sigma-Aldrich Inc. (Saint Louis, MO, USA).

4.2. Characterizations. The morphology and structure of all QDs were identified using a Talos F200C biological freezing transmission electron microscope (USA). After QDs were thoroughly mixed with dry KBr in a mortar and pressed into a pellet, the Fourier transform infrared (FT-IR) spectra of samples were recorded with an IR instrument model TENSOR 27 (Germany). Zeta potentials of $CuInS_2$-ZnS-GSH QDs and $CuInS_2$-ZnS-Cys QDs were measured by using the ZetaPALS BI-200SM (USA). The crystalline phase was performed on a Rigaku SmartLab X-ray diffractometer (Japan). The X-ray photoelectron spectra were obtained on a Kratos Axis Ultra DLD (Japan), and the instrument was calibrated against the C 1s band at 285 eV. The fluorescence analysis was performed on the F-4600 fluorophotometer (Japan). The UV−vis spectrum of QDs was recorded on UV-2450 UV−vis spectrophotometer (Japan). Cellular fluorescence images were obtained on ZeissLSM710 confocal laser scanning microscope.

4.3. Synthesis of $CuInS_2$-ZnS-GSH QDs. Typically, $InCl_3{\cdot}4H_2O$ (0.04 mmol), $CuCl_2{\cdot}2H_2O$ (0.01 mmol), and GSH (0.2 mmol) were separately dissolved in a 20 mL aqueous solution. After the pH of the solution was adjusted to 8.5 by the NaOH solution, the $Na_2S{\cdot}9H_2O$ (0.04 mmol) solution was added into the mixture and heated at 100 °C for 30 min. Sequentially, $Zn(Ac)_2$ (0.08 mmol) and $Na_2S{\cdot}9H_2O$ (0.04 mol) were added into the $CuInS_2$ solution and heated at 100 °C for 20 min. Then, a GSH solution was quickly added into the above reaction solution and heated at 100 °C for another 10 min. After being cooled down to room temperature, the QDs were purified with three repeated centrifugation steps at 10,000 rpm for 5 min by using deionized water and acetone alternately. The precipitate was finally dispersed in phosphate buffer solution or dried under vacuum for further investigation. The L-cysteine-capped $CuInS_2$-ZnS QDs were prepared in the same way.

4.4. The Fluorescence Detection of Cyt *c*. In a typical procedure, 400 μL of $CuInS_2$-ZnS-GSH QDs (30 μg mL^{-1}) was added into the various concentrations of Cyt *c* in the PBS solution (20 mM, pH 9.0). The fluorescence spectra of the incubated solution were recorded by a fluorophotometer. To investigate the selectivity of $CuInS_2$-ZnS-GSH QDs, several interfering substances, such as Mb, Hb, BSA, HSA, Lyz, metal ions, anions, and amino acids were added into the $CuInS_2$-ZnS-GSH QDs containing Cyt *c* at a concentration of 0.4 μmol L^{-1} and measured the fluorescent intensity under the same conditions, respectively.

4.5. Determination of Cyt *c* in the Serum Sample. The appropriate dilution (200-fold) of human serum and fetal bovine serum samples was chosen to evaluate the applicability of fluorescent $CuInS_2$-ZnS-GSH QDs for the determination of Cyt *c*.[53] First, the human serum or fetal bovine serum samples was centrifuged at 10,000 rpm for 3 min, using a high-speed freezing centrifuge. After that, each of the human serum and fetal bovine serum samples was diluted to 200-fold with the 20 mM phosphate buffer containing $CuInS_2$-ZnS-GSH QDs. Finally, the Cyt *c*-spiked serum sample solutions were directly analyzed using the fluorescent method.

https://doi.org/10.1021/acsomega.1c01983
ACS Omega 2021, 6, 17501−17509

4.6. Evaluation of Cytotoxicity. The cytotoxicity of $CuInS_2$-ZnS-GSH QDs was investigated by a standard MTT assay. HeLa cells were seeded in flat-bottom 96-well plate with 100 μL of DMEM medium and then incubated with various concentrations of $CuInS_2$-ZnS-GSH QDs at 37 °C for 24 h. After that, 10 μL of MTT (5 mg mL^{-1}) was added in HeLa cells for an additional 4 h, and then the medium was removed. The cell viability was determined and recorded for at least three times.

4.7. Cell Culture and Confocal Fluorescence Imaging. HeLa cells were cultured in Dulbecco's modified Eagle's medium supplemented with 10% FBS and 100 U/mL penicillin (1%)/streptomycin at 37 °C in a 100% humidified atmosphere (5% CO_2) for 24 h. After washing HeLa cells with 100 μL of DMEM three times, 15 μg mL^{-1} $CuInS_2$-ZnS-GSH QDs were incubated at 37 °C for another 2 h. Then, by using 25 mM Tris-HAc buffer (25 mM, pH 7.4, containing 125 mM of NaCl) for washing three times, the $CuInS_2$-ZnS-GSH QDs-stained HeLa cells were treated by different concentrations of etoposide (0, 10, 50, and 100 μmol L^{-1}) for 2 h at 37 °C. The HeLa cells were washed with the medium solution and fresh PBS to remove the remained etoposide and $CuInS_2$-ZnS-GSH QDs. Fluorescence imaging was recorded on ZeissLSM710 confocal laser scanning microscope.

■ ASSOCIATED CONTENT

Supporting Information

The Supporting Information is available free of charge at https://pubs.acs.org/doi/10.1021/acsomega.1c01983.

FT-IR spectrum of GSH and $CuInS_2$-ZnS-GSH QDs; XRD patterns of $CuInS_2$-ZnS and $CuInS_2$-ZnS-GSH QDs; the influence of the ZnS shell on the optical properties of $CuInS_2$ QDs; hydrodynamic diameter of $CuInS_2$ and $CuInS_2$-ZnS-GSH QDs; the zeta potential of $CuInS_2$-ZnS-GSH and $CuInS_2$-ZnS-Cys QDs; PL intensity change of $CuInS_2$-ZnS-GSH QDs during a period of 15 days; PL decay and PL lifetime of $CuInS_2$-ZnS-GSH QDs; effect of pH and incubated time on the detection of Cyt *c*; the selectivity response of $CuInS_2$-ZnS-GSH QDs; the toxicity of $CuInS_2$-ZnS-GSH QDs in HeLa cells; fluorescence spectra of $CuInS_2$-ZnS-GSH QDs in the presence of etoposide; and the comparison of methods for the determination of Cyt *c* (PDF)

■ AUTHOR INFORMATION

Corresponding Author

Langxing Chen − *College of Chemistry, Tianjin Key Laboratory of Biosensing and Molecular Recognition, and State Key Laboratory of Medicinal Chemical Biology, Nankai University, Tianjin 300071, P. R. China;* orcid.org/0000-0002-8616-9207; Email: lxchen@nankai.edu.cn

Authors

Xiangyang An − *College of Chemistry, Nankai University, Tianjin 300071, P. R. China*

Yuemei Zhang − *College of Chemistry, Nankai University, Tianjin 300071, P. R. China*

Jing Wang − *College of Chemistry, Nankai University, Tianjin 300071, P. R. China;* orcid.org/0000-0002-9100-6429

De-ming Kong − *College of Chemistry, Tianjin Key Laboratory of Biosensing and Molecular Recognition, and State Key Laboratory of Medicinal Chemical Biology, Nankai University, Tianjin 300071, P. R. China;* orcid.org/0000-0002-9216-8040

Xi-wen He − *College of Chemistry, Nankai University, Tianjin 300071, P. R. China*

Yukui Zhang − *College of Chemistry, Nankai University, Tianjin 300071, P. R. China; Dalian Institute of Chemical Physics, Chinese Academy of Sciences, Dalian 116023, P. R. China*

Complete contact information is available at: https://pubs.acs.org/10.1021/acsomega.1c01983

Notes

The authors declare no competing financial interest.

■ ACKNOWLEDGMENTS

This work was supported by the National Key Research and Development Program of China (no.2018YFC1602401), the National Natural Science Foundation of China (no. 22074067), and the Fundamental Research Funds for the Central Universities.

■ DEDICATION

Dedicated to the 100th anniversary of Chemistry at Nankai University.

■ REFERENCES

(1) Garrido, C.; Galluzzi, L.; Brunet, M.; Puig, P. E.; Didelot, C.; Kroemer, G. Mechanisms of cytochrome c release from mitochondria. *Cell Death Differ.* **2006**, *13*, 1423−1433.

(2) Wallace, D. C. Mitochondria and cancer. *Nat. Rev. Cancer* **2012**, *12*, 685−698.

(3) Li, Y.; He, K.; Huang, Y.; Zheng, D.; Gao, C.; Cui, L.; Jin, Y. H. Betulin induces mitochondrial cytochrome c release associated apoptosis in human cancer cells. *Mol. Carcinog.* **2010**, *49*, 630−640.

(4) Ouyang, L.; Shi, Z.; Zhao, S.; Wang, F. T.; Zhou, T. T.; Liu, B.; Bao, J. K. Programmed cell death pathways in cancer: a review of apoptosis, autophagy and programmed necrosis. *Cell Prolif.* **2012**, *45*, 487−498.

(5) Liu, Y.; Zhang, J.; Zuo, C.; Zhang, Z.; Ni, D.; Zhang, C.; Wang, J.; Zhang, H.; Yao, Z.; Bu, W. Upconversion nano-photosensitizer targeting into mitochondria for cancer apoptosis induction and cyt c fluorescence monitoring. *Nano Res.* **2016**, *9*, 3257−3266.

(6) Chen, T. T.; Tian, X.; Liu, C. L.; Ge, J.; Chu, X.; Li, Y. Fluorescence activation imaging of cytochrome c released from mitochondria using aptameric nanosensor. *J. Am. Chem. Soc.* **2015**, *137*, 982−989.

(7) Pandiaraj, M.; Sethy, N. K.; Bhargava, K.; Kameswararao, V.; Karunakaran, C. Designing label-free electrochemical immunosensors for cytochrome c using nanocomposites functionalized screen printed electrodes. *Biosens. Bioelectron.* **2014**, *54*, 115−121.

(8) Shamsipur, M.; Molaabasi, F.; Hosseinkhani, S.; Rahmati, F. Detection of Early Stage Apoptotic Cells Based on Label-Free Cytochrome c Assay Using Bioconjugated Metal Nanoclusters as Fluorescent Probes. *Anal. Chem.* **2016**, *88*, 2188−2197.

(9) Manickam, P.; Kaushik, A.; Karunakaran, C.; Bhansali, S. Recent advances in cytochrome c biosensing technologies. *Biosens. Bioelectron.* **2017**, *87*, 654−668.

(10) Ashe, D.; Alleyne, T.; Iwuoha, E. Serum cytochrome c detection using a cytochrome c oxidase biosensor. *Biotechnol. Appl. Biochem.* **2007**, *46*, 185−189.

(11) Crouser, E. D.; Gadd, M. E.; Julian, M. W.; Huff, J. E.; Broekemeier, K. M.; Robbins, K. A.; Pfeiffer, D. R. Quantitation of cytochrome c release from rat liver mitochondria. *Anal. Biochem.* **2003**, *317*, 67−75.

(12) Li, J.; Han, H.; Wang, Q.; Liu, X.; Jiang, S. Polymeric ionic liquid as a dynamic coating additive for separation of basic proteins by capillary electrophoresis. *Anal. Chim. Acta* **2010**, *674*, 243−248.
(13) Cummings, C.; Walder, J.; Treeful, A.; Jemmerson, R. Serum leucine-rich alpha-2-glycoprotein-1 binds cytochrome c and inhibits antibody detection of this apoptotic marker in enzyme-linked immunosorbent assay. *Apoptosis* **2006**, *11*, 1121−1129.
(14) Liao, D.; Chen, J.; Li, W.; Zhang, Q.; Wang, F.; Li, Y.; Yu, C. Fluorescence turn-on detection of a protein using cytochrome c as a quencher. *Chem. Commun.* **2013**, *49*, 9458−9460.
(15) Salehnia, F.; Hosseini, M.; Ganjali, M. R. A fluorometric aptamer based assay for cytochrome C using fluorescent graphitic carbon nitride nanosheets. *Microchim. Acta* **2017**, *184*, 2157−2163.
(16) Cao, L.; Li, X.; Qin, L.; Kang, S. Z.; Li, G. Graphene quantum dots supported by graphene oxide as a sensitive fluorescence nanosensor for cytochrome c detection and intracellular imaging. *J. Mater. Chem. B* **2017**, *5*, 6300−6306.
(17) Bera, D.; Qian, L.; Tseng, T.-K.; Holloway, P. H. Quantum Dots and Their Multimodal Applications: A Review. *Materials* **2010**, *3*, 2260−2345.
(18) Pietryga, J. M.; Park, Y.-S.; Lim, J.; Fidler, A. F.; Bae, W. K.; Brovelli, S.; Klimov, V. I. Spectroscopic and Device Aspects of Nanocrystal Quantum Dots. *Chem. Rev.* **2016**, *116*, 10513−10622.
(19) Coughlan, C.; Ibáñez, M.; Dobrozhan, O.; Singh, A.; Cabot, A.; Ryan, K. M. Compound Copper Chalcogenide Nanocrystals. *Chem. Rev.* **2017**, *117*, 5865−6109.
(20) Kundu, S.; Patra, A. Nanoscale Strategies for Light Harvesting. *Chem. Rev.* **2017**, *117*, 712−757.
(21) Sandroni, M.; Wegner, K. D.; Aldakov, D.; Reiss, P. Prospects of Chalcopyrite-Type Nanocrystals for Energy Applications. *ACS Energy Lett.* **2017**, *2*, 1076−1088.
(22) Li, X.; McNaughter, P. D.; O'Brien, P.; Minamimoto, H.; Murakoshi, K. Plasmonically Enhanced Electromotive Force of Narrow Bandgap PbS QD-based Photovoltaics. *Phys. Chem. Chem. Phys.* **2018**, *20*, 14818−14827.
(23) Chen, B.; Pradhan, N.; Zhong, H. Z. From Large-Scale Synthesis to Lighting Device Applications of Ternary I-III-VI Semiconductor Nanocrystals: Inspiring Greener Material Emitters. *J. Phys. Chem. Lett.* **2018**, *9*, 435−445.
(24) Biju, V.; Itoh, T.; Anas, A.; Sujith, A.; Ishikawa, M. Semiconductor quantum dots and metal nanoparticles: syntheses, optical properties, and biological applications. *Anal. Bioanal. Chem.* **2008**, *391*, 2469−2495.
(25) Kairdolf, B. A.; Smith, A. M.; Stokes, T. H.; Wang, M. D.; Young, A. N.; Nie, S. Semiconductor quantum dots for bioimaging and biodiagnostic applications. *Annu. Rev. Anal. Chem.* **2013**, *6*, 143−162.
(26) Knowles, K. E.; Hartstein, K. H.; Kilburn, T. B.; Marchioro, A.; Nelson, H. D.; Whitham, P. J.; Gamelin, D. R. Luminescent Colloidal Semiconductor Nanocrystals Containing Copper: Synthesis, Photophysics, and Applications. *Chem. Rev.* **2016**, *116*, 10820−10851.
(27) Corazzari, I.; Gilardino, A.; Dalmazzo, S.; Fubini, B.; Lovisolo, D. Localization of CdSe/ZnS Quantum Dots in the Lysosomal Acidic Compartment of Cultured Neurons and Its Impacton Viability: Potential Role of Ion Release. *Toxicol. In Vitro* **2013**, *27*, 752−759.
(28) Chang, L.; Wu, H.; He, X.; Chen, L.; Zhang, Y. A highly sensitive fluorescent turn-on biosensor for glycoproteins based on boronic acid functional polymer capped Mn-doped ZnS quantum dots. *Anal. Chim. Acta* **2017**, *995*, 91−98.
(29) Du, Y.; Guo, S. Chemically doped fluorescent carbon and graphene quantum dots for bioimaging, sensor, catalytic and photoelectronic applications. *Nanoscale* **2016**, *8*, 2532−2543.
(30) Li, X.; Rui, M.; Song, J.; Shen, Z.; Zeng, H. Carbon and Graphene Quantum Dots for Optoelectronic and Energy Devices: A Review. *Adv. Funct. Mater.* **2015**, *25*, 4929−4947.
(31) Li, L.; Daou, T. J.; Texier, I.; Kim Chi, T. T.; Liem, N. Q.; Reiss, P. Highly Luminescent CuInS/ZnS Core/Shell Nanocrystals: Cadmium-Free Quantum Dots for In Vivo Imaging. *Chem. Mater.* **2009**, *21*, 2422−2429.
(32) Shamirian, A.; Appelbe, O.; Zhang, Q.; Ganesh, B.; Kron, S. J.; Snee, P. T. A toolkit for bioimaging using near-infrared AgInS2/ZnS quantum dots. *J. Mater. Chem. B* **2015**, *3*, 8188−8196.
(33) Kolny-Olesiak, J.; Weller, H. Synthesis and Application of Colloidal CuInS2 Semiconductor Nanocrystals. *ACS Appl. Mater. Interfaces* **2013**, *5*, 12221−12237.
(34) Li, L.; Pandey, A.; Werder, D. J.; Khanal, B. P.; Pietryga, J. M.; Klimov, V. I. Efficient Synthesis of Highly Luminescent Copper Indium Sulfide-Based Core/Shell Nanocrystals with Surprisingly Long-Lived Emission. *J. Am. Chem. Soc.* **2011**, *133*, 1176−1179.
(35) Song, W.-S.; Yang, H. Efficient White-Light-Emitting Diodes Fabricated from Highly Fluorescent Copper Indium Sulfide Core/Shell Quantum Dots. *Chem. Mater.* **2012**, *24*, 1961−1967.
(36) Chen, B.; Zhong, H.; Zhang, W.; Tan, Z.; Li, Y.; Yu, C.; Zhai, T.; Bando, Y.; Yang, S.; Zou, B. Highly Emissive and Color-Tunable CuInS2-Based Colloidal Semiconductor Nanocrystals: Off-Stoichiometry Effects and Improved Electroluminescence Performance. *Adv. Funct. Mater.* **2012**, *22*, 2081−2088.
(37) Zhang, J.; Sun, W.; Yin, L.; Miao, X.; Zhang, D. One-pot synthesis of hydrophilic CuInS2 and CuInS2−ZnS colloidal quantum dots. *J. Mater. Chem. C* **2014**, *2*, 4812−4817.
(38) Pein, A.; Baghbanzadeh, M.; Rath, T.; Haas, W.; Maier, E.; Amenitsch, H.; Hofer, F.; Kappe, C. O.; Trimmel, G. Investigation of the formation of CuInS2 nanoparticles by the oleylamine route: comparison of microwave-assisted and conventional syntheses. *Inorg. Chem.* **2011**, *50*, 193−200.
(39) Qi, K.; Wang, Y.; Wang, R.; Wu, D.; Li, G. D. Facile synthesis of homogeneous CuInS2 quantum dots with tunable near-infrared emission. *J. Mater. Chem. C* **2016**, *4*, 1895−1899.
(40) Nam, D. E.; Song, W. S.; Yang, H. Facile, air-insensitive solvothermal synthesis of emission-tunable CuInS2/ZnS quantum dots with high quantum yields. *J. Mater. Chem.* **2011**, *21*, 18220−18226.
(41) Deng, D.; Chen, Y.; Cao, J.; Tian, J.; Qian, Z.; Achilefu, S.; Gu, Y. High-Quality CuInS2/ZnS Quantum Dots for In Vitro and In Vivo Bioimaging. *Chem. Mater.* **2012**, *24*, 3029−3037.
(42) De Mello Donegá, C.; Liljeroth, P.; Vanmaekelbergh, D. Physicochemical Evaluation of the Hot-Injection Method, a Synthesis Route for Monodisperse Nanocrystals. *Small* **2005**, *1*, 1152−1162.
(43) Nakamura, Y.; Iso, Y.; Isobe, T. Bandgap-Tuned CuInS2/ZnS Core/Shell Quantum Dots for a Luminescent Downshifting Layer in a Crystalline Silicon Solar Module. *ACS Appl. Nano Mater.* **2020**, *3*, 3417−3426.
(44) Choi, J.; Choi, W.; Jeon, D. Y. Ligand-Exchange-Ready CuInS2/ZnS Quantum Dots via Surface-Ligand Composition Control for Film-Type Display Devices. *ACS Appl. Nano Mater.* **2019**, *2*, 5504−5511.
(45) Wang, Q.; Fang, T.; Liu, P.; Deng, B.; Min, X.; Li, X. Direct synthesis of high-quality water-soluble CdTe:Zn2+ quantum dots. *Inorg. Chem.* **2012**, *51*, 9208−9213.
(46) Jindal, S.; Giripunje, S. M.; Kondawar, S. B.; Koinkar, P. Green synthesis of CuInS2/ZnS core-shell quantum dots by facile solvothermal route with enhanced optical properties. *J. Phys. Chem. Solids* **2018**, *114*, 163−172.
(47) Amin, R. M.; Elfeky, S. A.; Verwanger, T.; Krammer, B. Fluorescence-based CdTe nanosensor for sensitive detection of cytochrome C. *Biosens. Bioelectron.* **2017**, *98*, 415−420.
(48) Wen, Q.; Zhang, X.; Cai, J.; Yang, P. H. A novel strategy for real-time and in situ detection of cytochrome c and caspase-9 in Hela cells during apoptosis. *Analyst* **2014**, *139*, 2499−2506.
(49) Yan, Y. J.; He, X. W.; Li, W. Y.; Zhang, Y. K. Nitrogen-doped graphene quantum dots-labeled epitope imprinted polymer with double templates via the metal chelation for specific recognition of cytochrome c. *Biosens. Bioelectron.* **2017**, *91*, 253−261.
(50) Liu, J. M.; Yan, X. P. Ultrasensitive, selective and simultaneous detection of cytochrome c and insulin based on immunoassay and aptamer-based bioassay in combination with Au/Ag nanoparticle tagging and ICP-MS detection. *J. Anal. At. Spectrom.* **2011**, *26*, 1191−1197.

https://doi.org/10.1021/acsomega.1c01983
ACS Omega 2021, 6, 17501−17509

(51) Wang, J.; Wang, D. X.; Tang, A. N.; Kong, D. M. Highly Integrated, Biostable, and Self-Powered DNA Motor Enabling Autonomous Operation in Living Bodies. *Anal. Chem.* **2019**, *91*, 5244−5251.
(52) Robertson, J. D.; Enoksson, M.; Suomela, M.; Zhivotovsky, B.; Orrenius, S. Caspase-2 acts upstream of mitochondria to promote cytochrome c release during etoposide-induced apoptosis. *J. Biol. Chem.* **2002**, *277*, 29803−29809.
(53) Li, X.; Liu, H.; He, X.; Song, Z. Determination of cytochrome c in human serum and pharmaceutical injections using flow injection chemiluminescence. *Appl. Biochem. Biotechnol.* **2010**, *160*, 1065−1073.

https://doi.org/10.1021/acsomega.1c01983
ACS Omega 2021, 6, 17501−17509